Editors' Suggestion

Magnetooptics of Exciton Rydberg States in a Monolayer Semiconductor

A. V. Stier,[1] N. P. Wilson,[2] K. A. Velizhanin,[3] J. Kono,[4] X. Xu,[2] and S. A. Crooker[1]
[1]National High Magnetic Field Laboratory, Los Alamos, New Mexico 87545, USA
[2]Department of Physics, University of Washington, Seattle, Washington 98195, USA
[3]Theoretical Division, Los Alamos National Laboratory, Los Alamos, New Mexico 87545, USA
[4]Departments of Electrical and Computer Engineering, Physics and Astronomy, and Materials Science and NanoEngineering, Rice University, Houston, Texas 77005, USA

(Received 14 August 2017; published 1 February 2018)

We report 65 T magnetoabsorption spectroscopy of exciton Rydberg states in the archetypal monolayer semiconductor WSe_2. The strongly field-dependent and distinct energy shifts of the $2s$, $3s$, and $4s$ excited neutral excitons permits their unambiguous identification and allows for quantitative comparison with leading theoretical models. Both the sizes (via low-field diamagnetic shifts) and the energies of the ns exciton states agree remarkably well with detailed numerical simulations using the nonhydrogenic screened Keldysh potential for 2D semiconductors. Moreover, at the highest magnetic fields, the nearly linear diamagnetic shifts of the weakly bound $3s$ and $4s$ excitons provide a direct experimental measure of the exciton's reduced mass $m_r = 0.20 \pm 0.01 m_0$.

DOI: 10.1103/PhysRevLett.120.057405

The burgeoning interest in atomically thin transition-metal dichalcogenide (TMD) semiconductors such as monolayer MoS_2 and WSe_2 derives in part from their direct optical band gap and very strong light-matter coupling [1,2]. In a pristine TMD monolayer, the fundamental optical excitation—the ground-state neutral "A" exciton (X^0)—can, remarkably, absorb $> 10\%$ of incoming light [3]. Moreover, in doped or highly excited monolayers, distinct resonances due to charged excitons or multiexciton states can develop in optical spectra [4–9]. The ability to spectrally resolve these and other features depends critically on material quality, which has markedly improved in recent years as techniques for synthesis, exfoliation, and surface passivation have steadily progressed.

The optical quality of exfoliated WS_2 and WSe_2 monolayers has recently improved to the point where signatures of the much weaker *excited* Rydberg states of X^0 ($2s$, $2p$, $3s$, etc.) have been reported based on various linear and nonlinear optical spectroscopies [10–16]. Correct identification and quantitative measurements of excited excitons are of critical importance in this field because they provide direct insight into the *nonhydrogenic* attractive potential between electrons and holes that is believed to exist in 2D materials due to dielectric confinement and nonlocal screening [17–21]. This potential leads, for example, to an unconventionally spaced Rydberg series of excited excitons and can generate an anomalous ordering of (s, p, d) levels [10]. Crucially, these excited states allow one to directly estimate the free-particle band gap and binding energy of the X^0 ground state [10–15], both key material parameters that are otherwise difficult to measure in monolayer TMDs, and which are necessarily very sensitive to the surrounding dielectric environment [21–24]. Greatly desired, therefore, are incisive experimental tools for detailed studies of excited excitons in 2D semiconductors.

Historically, optical spectroscopy in high magnetic fields B has provided an especially powerful way to identify and quantify excited excitons [25–29], because each excited state shifts very differently with B. Crucially, these shifts can directly reveal fundamental parameters such as the exciton's mass, size, and spin—essential information for benchmarking theoretical models. For example, in the "weak-field limit," where the characteristic magnetic length $l_B = \sqrt{\hbar/eB}$ ($= 25.7/\sqrt{B}$ nm) is much larger than an exciton's radius, optically allowed excited excitons ($2s, 3s, ..., ns$) can be uniquely identified by their different *sizes*, which, in turn, are directly revealed via their quadratic diamagnetic shifts [25,26,30],

$$\Delta E_{\mathrm{dia}} = \frac{e^2}{8m_r}\langle r_\perp^2\rangle B^2 = \sigma B^2 \quad (\text{if } l_B \gg r_{ns}). \tag{1}$$

Here, $m_r = (m_e^{-1} + m_h^{-1})^{-1}$ is the exciton's reduced mass, σ is the diamagnetic coefficient, and $r_\perp$ is a radial coordinate perpendicular to B. The expectation value $\langle r_\perp^2\rangle = \langle \psi_{ns}|r_\perp^2|\psi_{ns}\rangle$ is calculated over the exciton's envelope wave function $\psi_{ns}(\mathbf{r})$. The exciton's root-mean-square (rms) radius is, therefore, $r_{ns} = \sqrt{\langle r_\perp^2\rangle} = \sqrt{8m_r\sigma}/e$. The key point is that excited states, being more loosely bound, are larger and therefore exhibit significantly larger diamagnetic shifts; e.g., in a 2D model with hydrogenlike

Coulomb potential ($\sim 1/r$), σ_{2s} and σ_{3s} are 39 and 275 times larger than σ_{1s}, respectively [28].

In the opposite "strong-field limit," where $l_B \ll r_{ns}$ and the spacing between Landau levels (LLs) exceeds typical binding energies, optically allowed interband transitions effectively occur between LLs in the valence and conduction bands. In conventional semiconductors, these transition energies, therefore, increase approximately linearly with B as $(N+\frac{1}{2})\hbar\omega_c^*$ (ignoring spin effects; $N = 0, 1, 2, \ldots$), where $\hbar\omega_c^* = \hbar eB/m_r$ is the exciton's cyclotron energy. Importantly, this provides a direct experimental measure of m_r, independent of any model. Finally, in the intermediate regime where $l_B \sim r_{ns}$, a gradual crossover of ΔE_{dia} from B^2 to B dependence is expected [25–29]. Magnetooptical studies of excited exciton states have a very successful history in III–V and II–VI semiconductors [25,26] and were employed 50 years ago to study bulk MoS_2 [31]. To date, however, high-field studies of Rydberg excitons in the new family of monolayer TMDs have not been reported.

Here we perform polarized magnetooptical spectroscopy to 65 T of monolayer WSe_2, an archetypal 2D semiconductor. The very different energy shifts of the $2s$, $3s$, and $4s$ excited states of X^0 are observed and studied for the first time. This permits not only their unambiguous identification but also allows for direct quantitative comparison with leading theoretical models based on the nonhydrogenic screened Keldysh potential [19–21]. A value of m_r is experimentally obtained.

Figure 1(a) depicts the experiment. To achieve high optical quality, a single WSe_2 monolayer was sandwiched between 10 nm thick hexagonal boron nitride (hBN) slabs using a dry-transfer process and exfoliated materials. The assembly was then affixed over the 3.5 μm diameter core of a single-mode optical fiber to ensure a rigid optical alignment. The fiber was mounted in the low-temperature (4 K) bore of a 65 T pulsed magnet. Broadband white light from a Xe lamp was coupled through the structure via the single-mode fiber, and the transmitted light passed through a thin-film circular polarizer before being redirected back into a separate collection fiber. The collected light was dispersed in a 300 mm spectrometer and detected with a CCD detector. Spectra were acquired every 2.3 ms throughout the magnet pulse, following Ref. [23]. Access to σ^- or σ^+ circularly polarized optical transitions (corresponding to transitions in the K or K' valley of WSe_2) was achieved by reversing B.

Figure 1(b) shows normalized transmission spectra (T/T_0) at 0, 30, 45, and 65 T. At $B = 0$, the strong and narrow absorption line at 1.723 eV corresponds to the well-known ground ($1s$) state of X^0. In addition, a weaker absorption also appears 130 meV higher in energy, at 1.853 eV. This feature has been observed in several studies of hBN-encapsulated WSe_2 monolayers [6,32–35], and has been ascribed either to the excited $2s$ state of X^0 [32,33], or

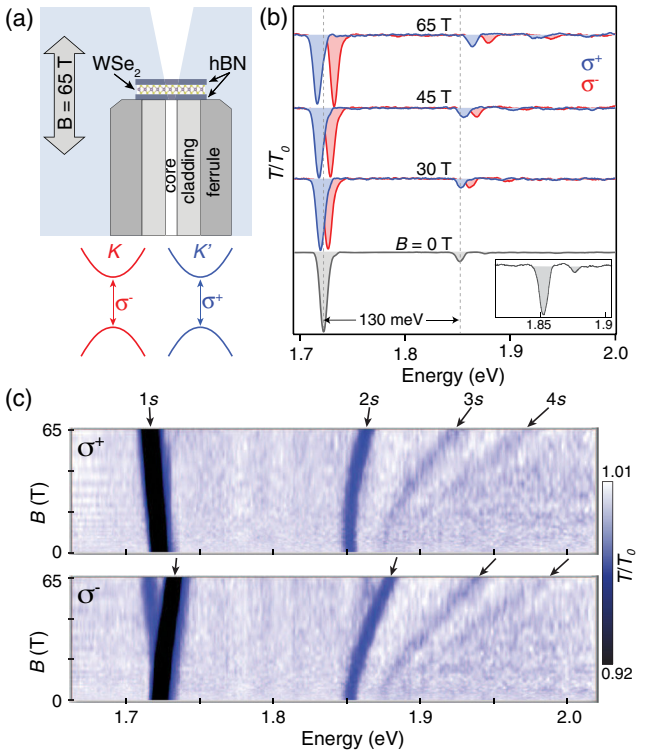

FIG. 1. (a) Experimental schematic: A WSe_2 monolayer sandwiched between hBN slabs is positioned over the 3.5 μm diameter core of a single-mode optical fiber. Circularly polarized $\sigma^{\pm}$ transmission spectra are acquired to 65 T at low temperature (4 K). (b) Normalized transmission spectra T/T_0 at selected magnetic fields B from 0 to 65 T. The $1s$ ground state of the neutral A exciton X^0 appears at 1.723 eV. Its $2s$ excited state is also clearly visible at 1.853 eV (130 meV higher in energy); it exhibits a much larger diamagnetic blueshift in accordance with its much larger spatial extent (vertical dashed lines indicate their zero-field energies). Inset: The $3s$ excited state is faintly visible even at $B = 0$. (c) Intensity plots showing all the $\sigma^{\pm}$ spectra from 0–65 T. The large shifts of the weak $3s$ and $4s$ states of X^0 are readily apparent. (A small amount of σ^+ polarization leaks into the σ^- spectra, especially for the strong $1s$ feature at large B).

alternatively, to a composite exciton-phonon resonance consisting of hBN and WSe_2 phonons coupled to the X^0 ground state [34,35]. A central goal of this work is to elucidate the nature of this and other higher-energy states based on their evolution in large B.

As B increases to 65 T, Fig. 1(b) shows that these absorption features split and shift. The Zeeman splitting and small diamagnetic shift of the X^0 ground state were observed previously in monolayer WSe_2 [23], albeit using different encapsulations. The similar splitting but much larger blueshift of the higher-energy absorption are clearly seen. Moreover, these spectra also reveal weak *additional* features developing at even higher energy. To best visualize these changes, Fig. 1(c) shows an intensity map of all the T/T_0 spectra from 0–65 T. A key result is that, in addition to the X^0 ground state and the smaller absorption at

1.853 eV, two additional absorption features are clearly discerned at higher energies that blueshift even more rapidly with B. Based on their shifts and splittings (quantified in detail below), we can unambiguously associate these four features with the optically allowed $1s$, $2s$, $3s$, and $4s$ Rydberg states of X^0.

Figure 2(a) quantifies these trends and shows the field-dependent $\sigma^{\pm}$ energies of these excitons, which follow $E(B) = E_0 + \Delta E_{\mathrm{dia}} \pm g_v \mu_B B$, where the last term describes the valley-dependent Zeeman splitting due to the exciton's magnetic moment [30]. The similar Zeeman splittings but very different diamagnetic shifts of the ns excitons are readily apparent in Fig. 2(a). Figure 2(c) shows the energy *differences* between the $\sigma^{\pm}$ absorption peaks, revealing similar Zeeman splittings of $\sim$245 μeV/T, equivalent to a valley g factor $g_v \simeq -4.2$ for the $1s$ state of X^0 (in reasonable agreement with prior studies [23,36–38]) and also for the ns excited states (measured here for the first time in a monolayer TMD). This concurrence is noteworthy because, as shown immediately below, the *size* of these ns excitons varies significantly by over an order of magnitude. Therefore, their similar g_v values point to a rather homogeneous distribution of orbital magnetism and Berry curvature in reciprocal space about the K and K' points of the Brillouin zone, in agreement with early theoretical studies of monolayer TMDs [39].

Most importantly, Fig. 2(b) shows the *average* energy of the $\sigma^{\pm}$ absorption peaks for each ns state, which reveals the diamagnetic shifts alone (independent of valley Zeeman effects). The shift of the $1s$ exciton is small and purely quadratic ($\sigma_{1s} = 0.31 \pm 0.02$ μeV/T^2, in line with recent studies of encapsulated WSe_2 [23]) and directly reveals its small rms radius $r_{1s} = 1.7 \pm 0.1$ nm via Eq. (1). (Here, we use $m_r = 0.20 m_0$, which is slightly larger than predicted by theory [19,21]; however, this value is consistent with modeling of σ_{1s} [40], and as shown below, it is independently recommended by the high-field shifts of the $3s/4s$ states.) In marked contrast to the $1s$ state, the quadratic shift of the $2s$ state is $\sim$15$\times$ larger ($\sigma_{2s} = 4.6 \pm 0.2$ μeV/T^2), confirming that the $2s$ exciton has a considerably larger radius $r_{2s} \simeq \sqrt{15} r_{1s} \simeq 6.6$ nm. Continuing, the $3s$ state exhibits an even more pronounced blueshift that follows B^2 up to 25 T. In this range, $\sigma_{3s} = 22 \pm 2$ μeV/T^2, which is $\sim$71$\times$ larger than σ_{1s}, indicating that $r_{3s} \simeq \sqrt{71} r_{1s} = 14.3 \pm 1.5$ nm. These ratios ($\sigma_{2s}/\sigma_{1s} = 15$ and $\sigma_{3s}/\sigma_{1s} = 71$) are *significantly* different than ratios expected from a hydrogenic exciton model in two dimensions (39 and 275, respectively [28]), confirming that the effective Coulomb potential in real monolayer semiconductors deviates markedly from $1/r$.

Above 30 T, the $3s$ (and $4s$) energy shifts depart from B^2 and evolve toward a more linear dependence on B, indicating a crossover to the intermediate-field regime where $l_B \sim r_{3s}(r_{4s})$. As discussed below and at length in the Supplemental Material [40], their nearly linear shifts at large B can be used to experimentally determine m_r, values

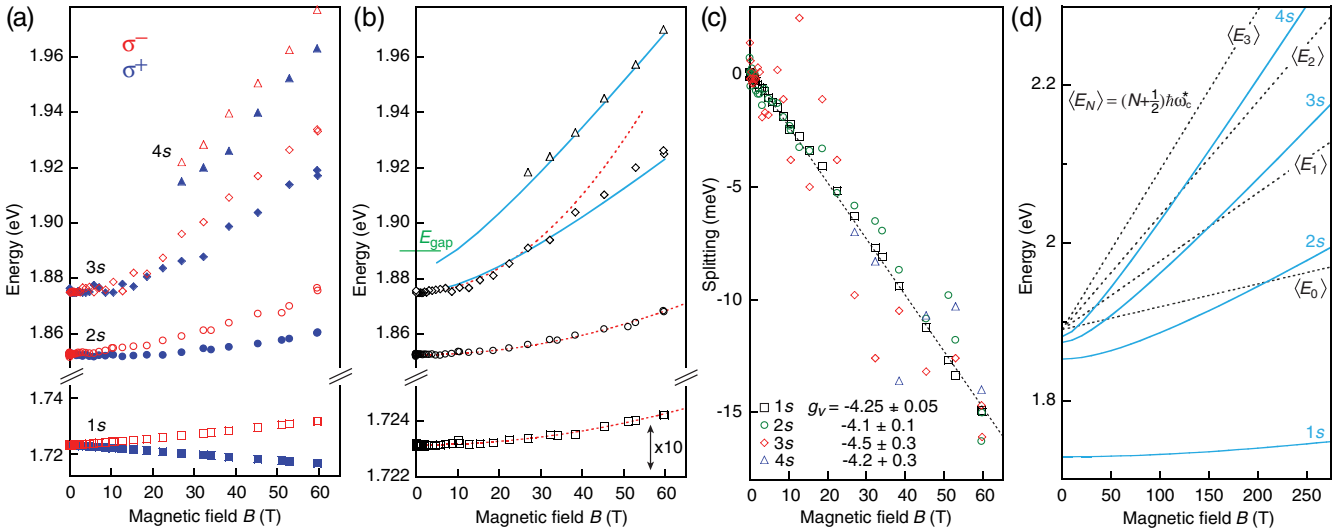

FIG. 2. (a) Measured $1s$, $2s$, $3s$, and $4s$ exciton energies versus B, for both σ^+ and σ^- polarizations. (b) The *average* energy of the $\sigma^{\pm}$ transitions for all the ns states (note 10$\times$ vertical scale for the $1s$ state). Dotted red lines show purely quadratic fits to B^2. The quadratic shifts of the $2s$ and $3s$ states are 15$\times$ and 71$\times$ larger than that of $1s$, quantitatively consistent with their larger radii computed from theory. The $3s$ and $4s$ states evolve toward a more linear shift at large B, which can be calculated numerically in this intermediate-field regime [40]. Blue lines show the numerically calculated $3s/4s$ energies using $m_r = 0.2 m_0$. (c) The $\sigma^{\pm}$ energy difference reveals a similar valley Zeeman splitting for all ns states. The dotted straight line has slope -245 μeV/T ($g_v \approx -4.2$). (d) The blue lines show numerically calculated energies for all ns Rydberg excitons to very large B. The straight dashed lines show $\langle E_N \rangle = (N + \frac{1}{2})\hbar\omega_c^*$, the valley-averaged energies of interband transitions between free electron and hole LLs [40]. At very large B, the slope of the ns exciton shift approaches that of $\langle E_N \rangle$, where $N = n - 1$.

for which, to date, have been inferred primarily from density-functional theory [19,21]. We note further that the oscillator strengths of the $3s$ and $4s$ excitons increase at large B [see Fig. 1(c)], in accordance with expectation [27].

First, however, we show that the 15× and 71× larger diamagnetic shifts of the $2s$ and $3s$ excitons—and also their zero-field energies of 130 and 152 meV above the $1s$ ground state—agree remarkably well with straightforward modeling using the nonhydrogenic Keldysh potential that is believed to best describe electron-hole attraction in a monolayer material confined between dielectric slabs [17–21]:

$$V_K(r) = -\frac{e^2}{8\varepsilon_0 r_0}\left[H_0\left(\frac{\kappa r}{r_0}\right) - Y_0\left(\frac{\kappa r}{r_0}\right)\right]. \quad (2)$$

Here, H_0 and Y_0 are the Struve and Bessel functions of the second kind. The dielectric nature of the WSe_2 monolayer is characterized by its screening length $r_0 = 2\pi\chi_{2D}$, where χ_{2D} is the 2D polarizability. We use $r_0 = 4.5$ nm, consistent with theory [19,21] and experimental work [23]. The encapsulating hBN slabs are captured by κ, the average dielectric constant of the surrounding material: $\kappa = \frac{1}{2}(\epsilon_{\text{top}} + \epsilon_{\text{bottom}})$. We use high-frequency (infrared) dielectric constants because the characteristic frequency at which a dielectric responds to an exciton is given roughly by its binding energy [26,49], which is large in TMD monolayers. Thus, we use $\kappa_{\text{hBN}} = 4.5$ based on infrared measurements [50]. $V_K(r)$ scales as $1/\kappa r$ when $r \gg r_0$ but diverges only weakly as $\log(r)$ when $r \ll r_0$ due to increased screening from the 2D material itself. Equation (2) is often used to model excitons in monolayer materials [12,19–21], and it approximates reasonably well the potentials derived from more advanced models [22,32].

The black curve in Fig. 3(a) shows $V_K(r)$. Also shown are $\psi_{ns}(r)$, the ns wave functions of X^0 calculated numerically via Schrödinger's equation using $m_r = 0.20m_0$. The $1s$ ground state has a calculated binding energy of 161 meV and radius $r_{1s} = \sqrt{\langle\psi_{1s}|r_\perp^2|\psi_{1s}\rangle} = 1.67$ nm, which is very close to the value of 1.7 nm that was directly measured [in Fig. 2(b)] from σ_{1s}. Most importantly, we calculated $r_{2s} = 6.96$ nm and $r_{3s} = 15.8$ nm, which agree rather well (within 10%) with the values of 6.6 and 14.3 nm that were directly measured from their diamagnetic shifts. Put another way, σ_{2s} and σ_{3s} in hBN-encapsulated monolayer WSe_2 are predicted to be 17× and 89× larger than σ_{1s}, in reasonable agreement with the 15× and 71× larger diamagnetic shifts that are experimentally measured, confirming their identity.

This interpretation is further supported by Fig. 3(b), which shows the calculated binding energies of the ns excitons versus κ. The calculated $1s-2s$ and $2s-3s$ energy differences are 124 and 21.3 meV, respectively, when $\kappa = \kappa_{\text{hBN}} = 4.5$ [50]. These values agree closely with the experimentally measured separations of 130 and 22 meV, further confirming the nature of these Rydberg

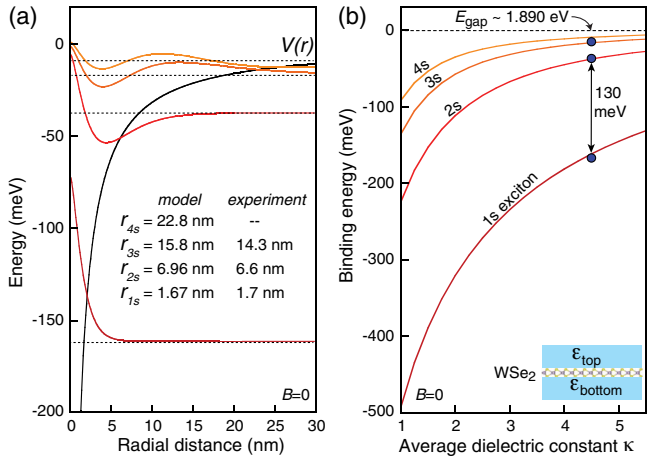

FIG. 3. (a) Plots of $\psi_{ns}(r)$, the $1s$, $2s$, $3s$, and $4s$ wave functions of X^0 in an hBN-encapsulated WSe_2 monolayer, computed using $V_K(r)$ (black line), using $r_0 = 4.5$ nm, $\kappa_{\text{hBN}} = 4.5$, and $m_r = 0.20m_0$. The calculated rms exciton radii $r_{ns} = \sqrt{\langle\psi_{ns}|r_\perp^2|\psi_{ns}\rangle}$ are close to experimental values. Crucially, we note that a rms radius is *not* the same as a "Bohr radius"; in the context of 3D (2D) hydrogenic models, rms radii are larger by a factor of $\sqrt{2}$ ($\sqrt{1.5}$) [30]. Thus, the $1s$ rms exciton radius in *bulk* WSe_2 was reported [51] to be $\sqrt{2} \times 1.8$ nm $= 2.54$ nm. (b) Calculated ns exciton binding energies versus κ. When $\kappa = 4.5$, the calculated $1s-2s$ and $2s-3s$ separations are 124 and 21.3 meV, very close to the experimental values of 130 and 22 meV. Correlating the model with the data (dark blue points) indicates a free-particle gap of ~1.890 eV for hBN/WSe_2/hBN.

states and the applicability of $V_K(r)$ to monolayer TMDs. Overlapping the model with the measured exciton energies (blue points), we infer a free-particle band gap $E_{\text{gap}} \approx 1.890$ eV for hBN/WSe_2/hBN.

Finally, we analyze the high-B shifts of the $3s/4s$ excitons [Fig. 2(b)] to determine m_r, the reduced mass of X^0—a key material parameter that to date has not been directly measured. However, even at 65 T these excitons are only in the intermediate-field regime where their shifts are still evolving from quadratic to linear in B, and their energies lack simple analytic forms [25–29]. Nonetheless, the *slopes* and *separation* of the $3s/4s$ states at high B provide upper and lower bounds on m_r, respectively [40]. The slope of the $4s$ shift, which should eventually *increase* to $(7/2)\hbar\omega_c^*/B$ [see Fig. 2(d)], is ~1.77 meV/T at 60 T, yielding an upper bound $m_r < 0.23m_0$. Conversely, the ratio $\delta/\hbar\omega_c^*$, where δ is the $3s-4s$ separation, should eventually *decrease* to unity. We measure $\delta \sim 34$ meV at 60 T, giving a lower bound of $m_r > 0.16m_0$.

Tighter bounds on m_r are obtained in this difficult intermediate-field regime by computing the exciton energies directly. However, analytical approximations have considered only hydrogenlike potentials [27,28]. Therefore, we numerically computed [40] the B-dependent exciton wave functions and energies using the relevant Hamiltonian for s

states in 2D semiconductors, $H = -(\hbar^2/2m_r)\nabla_r^2 + e^2B^2r^2/8m_r + V_K(r)$. In Fig. 2(b), we overlay these numerical results for the $3s$ and $4s$ states with the data. A best fit is obtained using $m_r = 0.20 \pm 0.01 m_0$ (about 15% larger than predicted by recent theory [19,21]), thereby providing an internally consistent experimental measure of X^0's reduced mass in a monolayer TMD.

Figure 2(d) shows the numerical results for all ns states to very high B (> 250 T). Also plotted are the valley-averaged energies of the optically allowed interband transitions between free-particle LLs, $\langle E_N \rangle = \frac{1}{2}(E_N^K + E_N^{K'}) = (N + \frac{1}{2})\hbar\omega_c^*$ ($N = 0, 1, 2, ...$), which are analogous to inter-LL transitions in conventional semiconductors (for details, see the Supplemental Material [40]). Only at extremely large B ($\gg 100$ T) are the ns exciton shifts approximately parallel to those of $\langle E_N \rangle$ (where $N = n - 1$), indicating the strong-field limit. Note that due to the exciton binding energy, an offset always exists between the ns exciton energy and the corresponding $\langle E_N \rangle$ energy.

In summary, 65 T magnetoabsorption spectroscopy was used to identify and quantify the optically allowed ns Rydberg states of neutral excitons in a monolayer semiconductor. The distinct shifts of the different ns states allowed for direct quantitative comparison between experiment and theory. Both the sizes and energies of the ns excitons are in good agreement with the screened Keldysh potential, and, furthermore, the nearly linear energy shifts of the most weakly bound excitons provided an experimental measure of the exciton mass itself. Future studies using larger magnetic fields and/or higher-quality monolayers in which even higher Rydberg states are visible can further improve these bounds in WSe_2 and other members of the monolayer TMD family.

We thank B. Urbaszek, X. Marie, and Wang Yao for helpful discussions. Work at the National High Magnetic Field Laboratory (NHMFL) was supported by National Science Foundation (NSF) Grant No. DMR-1157490, the State of Florida, and the U.S. Department of Energy (DOE). Work at the University of Washington was supported by the Department of Energy, Basic Energy Sciences, Materials Sciences and Engineering Division (Grant No. DE-SC0018171). K. A. V. was supported by the Department of Energy, Basic Energy Sciences, Energy Frontier Research Center (DOE BES EFRC) program. J. K. was supported by Air Force Office of Science Research (AFOSR) Grant No. FA9550-14-1-0268.

A. V. S. and N. P. W. contributed equally to this work.

[1] K. F. Mak and J. Shan, Nat. Photonics **10**, 216 (2016).
[2] X. Xu, W. Yao, D. Xiao, and T. F. Heinz, Nat. Phys. **10**, 343 (2014).
[3] Y. Li, A. Chernikov, X. Zhang, A. Rigosi, H. M. Hill, A. M. van der Zande, D. A. Chenet, E. M. Shih, J. Hone, and T. F. Heinz, Phys. Rev. B **90**, 205422 (2014).
[4] J. S. Ross, S. Wu, H. Yu, N. J. Ghimire, A. M. Jones, G. Aivazian, J. Yan, D. G. Mandrus, D. Xiao, W. Yao, and X. Xu, Nat. Commun. **4**, 1474 (2013).
[5] Z. Wang, J. Shan, and K. F. Mak, Nat. Nanotechnol. **12**, 144 (2016).
[6] E. Courtade, M. Semina, M. Manca, M. M. Glazov, C. Robert, F. Cadiz, G. Wang, T. Taniguchi, K. Watanabe, M. Pierre, W. Escoffier, E. L. Ivchenko, P. Renucci, X. Marie, T. Amand, and B. Urbaszek, Phys. Rev. B **96**, 085302 (2017).
[7] Y. You, X. X. Zhang, T. C. Berkelbach, M. S. Hybertsen, D. R. Reichman, and T. F. Heinz, Nat. Phys. **11**, 477 (2015).
[8] M. Szyniszewski, E. Mostaani, N. D. Drummond, and V. I. Fal'ko, Phys. Rev. B **95**, 081301(R) (2017).
[9] K. Hao *et al.*, Nat. Commun. **8**, 15552 (2017).
[10] Z. Ye, T. Cao, K. O'Brien, H. Zhu, X. Yin, Y. Wang, S. G. Louie, and X. Zhang, Nature (London) **513**, 214 (2014).
[11] K. He, N. Kumar, L. Zhao, Z. Wang, K. F. Mak, H. Zhao, and J. Shan, Phys. Rev. Lett. **113**, 026803 (2014).
[12] A. Chernikov, T. C. Berkelbach, H. M. Hill, A. Rigosi, Y. Li, O. B. Aslan, D. R. Reichman, M. S. Hybertsen, and T. F. Heinz, Phys. Rev. Lett. **113**, 076802 (2014).
[13] B. Zhu, X. Chen, and X. Cui, Sci. Rep. **5**, 9218 (2015).
[14] G. Wang, X. Marie, I. Gerber, T. Amand, D. Lagarde, L. Bouet, M. Vidal, A. Balocchi, and B. Urbaszek, Phys. Rev. Lett. **114**, 097403 (2015).
[15] H. M. Hill, A. F. Rigosi, C. Roquelet, A. Chernikov, T. C. Berkelbach, D. R. Reichman, M. S. Hybertsen, L. E. Brus, and T. F. Heinz, Nano Lett. **15**, 2992 (2015).
[16] T. Stroucken and S. W. Koch, J. Phys. Condens. Matter **27**, 345003 (2015).
[17] L. V. Keldysh, JETP Lett. **29**, 658 (1979).
[18] P. Cudazzo, I. V. Tokatly, and A. Rubio, Phys. Rev. B **84**, 085406 (2011).
[19] T. C. Berkelbach, M. S. Hybertsen, and D. R. Reichman, Phys. Rev. B **88**, 045318 (2013).
[20] F. Wu, F. Qu, and A. H. MacDonald, Phys. Rev. B **91**, 075310 (2015).
[21] I. Kylänpää and H.-P. Komsa, Phys. Rev. B **92**, 205418 (2015).
[22] S. Latini, T. Olsen, and K. S. Thygesen, Phys. Rev. B **92**, 245123 (2015).
[23] A. V. Stier, N. P. Wilson, G. Clark, X. Xu, and S. A. Crooker, Nano Lett. **16**, 7054 (2016).
[24] A. Raja *et al.*, Nat. Commun. **8**, 15251 (2017).
[25] N. Miura, *Physics of Semiconductors in High Magnetic Fields* (Oxford University Press, New York, 2008).
[26] R. S. Knox, *Theory of Excitons* (Academic Press, New York, 1963).
[27] O. Akimoto and H. Hasegawa, J. Phys. Soc. Jpn. **22**, 181 (1967).
[28] A. H. MacDonald and D. S. Ritchie, Phys. Rev. B **33**, 8336 (1986).
[29] W. Edelstein, H. N. Spector, and R. Marasas, Phys. Rev. B **39**, 7697 (1989).
[30] A. V. Stier, K. M. McCreary, B. T. Jonker, J. Kono, and S. A. Crooker, Nat. Commun. **7**, 10643 (2016).

[31] B. L. Evans and P. A. Young, Proc. Phys. Soc. London **91**, 475 (1967).
[32] B. Scharf, Z. Wang, D. Van Tuan, J. Shan, K. F. Mak, I. Zutic, and H. Dery, arXiv:1606.07101.
[33] M. Manca, M. M. Glazov, C. Robert, F. Cadiz, T. Taniguchi, K. Watanabe, E. Courtade, T. Amand, P. Renucci, X. Marie, G. Wang, and B. Urbaszek, Nat. Commun. **8**, 14927 (2017).
[34] C. M. Chow, H. Yu, A. M. Jones, J. Yan, D. G. Mandrus, T. Taniguchi, K. Watanabe, W. Yao, and X. Xu, Nano Lett. **17**, 1194 (2017).
[35] C. Jin, J. Kim, J. Suh, Z. Shi, B. Chen, Z. Fan, M. Kam, K. Watanabe, T. Taniguchi, S. Tongay, A. Zettl, J. Wu, and F. Wang, Nat. Phys. **13**, 127 (2017).
[36] A. Srivastava, M. Sidler, A. V. Allain, D. S. Lembke, A. Kis, and A. Imamoğlu, Nat. Phys. **11**, 141 (2015).
[37] G. Wang, L. Bouet, M. M. Glazov, T. Amand, E. L. Ivchenko, E. Palleau, X. Marie, and B. Urbaszek, 2D Mater. **2**, 034002 (2015).
[38] A. A. Mitioglu, P. Plochocka, A. Granados del Aguila, P. C. M. Christianen, G. Deligeorgis, S. Anghel, L. Kulyuk, and D. K. Maude, Nano Lett. **15**, 4387 (2015).
[39] T. Cao *et al.*, Nat. Commun. **3**, 887 (2012).
[40] See the Supplemental Material at http://link.aps.org/supplemental/10.1103/PhysRevLett.120.057405 for a detailed discussion of Landau levels, *ns* exciton energies, exciton mass, Dirac Hamiltonian, nonparabolicity, and dielectric effects, which includes Refs. [41–48].
[41] D. Xiao, G.-B. Liu, W. Feng, X. Xu, and W. Yao, Phys. Rev. Lett. **108**, 196802 (2012).
[42] F. Rose, M. O. Goerbig, and F. Piechon, Phys. Rev. B **88**, 125438 (2013).
[43] A. Srivastava and A. Imamoğlu, Phys. Rev. Lett. **115**, 166802 (2015).
[44] J. Zhou, W.-Y. Shan, W. Yao, and D. Xiao, Phys. Rev. Lett. **115**, 166803 (2015).
[45] S. N. Walck and T. L. Reinecke, Phys. Rev. B **57**, 9088 (1998).
[46] X. Li, F. Zhang, and Q. Niu, Phys. Rev. Lett. **110**, 066803 (2013).
[47] R.-L. Chu, X. Li, S. Wu, Q. Niu, W. Yao, X. Xu, and C. Zhang, Phys. Rev. B **90**, 045427 (2014).
[48] M. Bieniek, M. Korkusinski, L. Szulakowska, P. Potasz, I. Ozfidan, and P. Hawrylak, arXiv:1705.02917 [Phys. Rev. B (to be published)].
[49] F. Bechstedt, *Many-Body Approach to Electronic Excitations* (Springer-Verlag, Berlin, 2015).
[50] R. Geick, C. H. Perry, and G. Rupprecht, Phys. Rev. **146**, 543 (1966).
[51] A. R. Beal and W. Y. Liang, J. Phys. C: Solid State Phys. **9**, 2459 (1976).